This article has been accepted for publication in IEEE Transactions on Instrumentation and Measurement. This is the author's version which has not been fully edited and content may change prior to final publication. Citation information: DOI 10.1109/TIM.2024.3428592

"3-2-1" PMP: Adding an Extra Pattern to Dual-Band Phase-Shift Profilometry for Higher Precision 3D Imaging

Jian Wang, Member, IEEE, Guanyu Zhang, Wei Guo, Jun Zhang, Zonghua Zhang, Liangzhou Chen, Tukun Li, and Xiangqian Jiang

***Abstract*—Phase measurement profilometry, or PMP, is undergoing rapid development at present. Combined with defocused projection and advanced multi-band phase-shift algorithms, such as heterodyne and number theory, PMP with over thousand framerates has shown great potential in three-dimensional dynamic scene monitoring, e.g., manufacturing process monitoring and industrial digital twins. PMP's outstanding advantages include a combination of high lateral resolution, axial precision, and speed; however, the widely used dual-band phase-shift algorithms have limited axial precision compared to low-efficiency tri-band algorithms. In this paper, we propose "3-2-1" PMP, which optimizes the existing dual-band approach by adding an extra fringe pattern for projection acquisition to achieve similar precision performance as tri-band PMP. Associated stabilization algorithms in dealing with fringe blur, nonlinear camera responses, phase-jump errors, and related impact factors have also been investigated. Comparative simulation and experiments show that the "3-2-1" approach produces higher precision performance, with a 42%-85% root-mean-square error lower than general dual-band phase-shift methods and famous μFTP, but using an equivalent projection pattern number of 6 or less.**

***Index Terms*—Fringe projection profilometry, 3D imaging, pattern optimization, calibration, fringe order error.**

I. Introduction

Phase measurement profilometry, or PMP for short, as a subclass of fringe projection profilometry, acquires fringe phase maps of an object or scene for three-dimensional (3D) reconstruction. With outstanding lateral resolution, axial accuracy, and speed, PMP has been recognized as a powerful tool for dynamic sensing applications, including 3D robot vision, manufacturing metrology, industrial digital twins, and medical diagnosis [1-4]. For example, melt-pool solidification process monitoring regarding topography evolution was recently realized to predict additive manufacturing subsurface defects and stress, with the assistance of finite element analysis [5]. Among the advanced applications, simultaneous high sensing speed and accuracy are required to guarantee measurement accuracy and instant feedback control.

Numerous methods have been developed to address PMP accuracy and speed problems, among which optimization of fringe patterns and process algorithms is an important approach and constitutes an essential supplement to hardware modifications [6, 7]. For example, Fourier transform profilometry (FTP) [10, 11] based on spatial spectral filtration, has been developed for high-speed sensing with uncertain accuracy. Phase-shift profilometry (PSP), which measures phases through a temporal signal analysis, overcomes the spatial-spectral dependence of FTP and has been used for high-accuracy imaging applications [12, 13]. Sinusoidal fringes produced from defocused binary patterns successfully maximized the projection speed of widely used digital mirror array projectors [8, 9]. Performance optimized PMP through RGB multi-channel imaging [14, 15], geometrical constraints [16, 17], and the latest machine learning [18] were also investigated. From the perspective of technical maturity, triple-band or frequency [10, 19] sinusoidal fringe patterns with three, four, or more steps of phase shifts are most welcome in high-accuracy PMP. Dual-band or bi-band three steps of phase-shifts (3-PS) [12, 20] could be the most widely used approach in high-speed PMP. The former requires typically "3-3-3" or "4-4-4" (refer to I.A for more details) patterns of projection in total; the latter requires "3-3" or fewer patterns in total. However, none of them can guarantee both accuracy and speed. A brief literature review of the recent PMP based on phase-shifts development is provided in the following. Readers can refer to the latest review papers [1, 21, 22] for more details.

A. Related Work

FTP, based on Fourier transform analyses of a fringe image or image stack, is the most popular in high-speed applications. FTP extracts the base-frequency component modulated by spatial

Manuscript received Month xx, 2xxx; revised Month xx, xxxx; accepted Month x, xxxx. This project is supported by National Natural Science Foundation of China (No. 52075206, U2341275), National Key Research & Development Program (No. 2023YFB4606000), and Knowledge Innovation Program of Wuhan-Basic Research.

J. Wang, G. Zhang, W. Guo, and L. Chen are with the State Key Lab of Intelligent Manufacturing Equipment and Technology, Huazhong University of Science and Technology, Wuhan 430074, China (e-mail: jianwang@hust.edu.cn; guanyuzhang@hust.edu.cn; weig@hust.edu.cn; chenlz@hust.edu.cn).

J. Zhang (corresponding author) is with the School of Information Engineering, Guangdong University of Technology, Guangzhou 510006, PR China (email: jzhang@gdut.edu.cn)

Z. Zhang (corresponding author) is with the School of Mechanical Engineering, Hebei University of Technology, Tianjin 300130, PR China (e-mail: zhzhang@hebut.edu.cn).

T. Li and X. Jiang are with EPSRC Future Metrology Hub, University of Huddersfield, HD1 3DH Huddersfield, U.K. (e-mail: t.li@hud.ac.uk; x.jiang@hud.ac.uk).

sinusoidal fringes from a Fourier spectrum and then reversely transforms it to the spatial domain for phase calculation [23]. Since 2002, Zhang et al. [24, 25] pioneered FTP research in dynamic imaging of vibrating loudspeakers and micro-air-vehicle flapping wings. To overcome the problem of spectral aliasing and non-uniform background reflections, advanced FTP methods, including π-shift FTP, modified FTP, and background-normalized FTP (BNFTP) were developed [10], in which an additional fringe pattern was required; thus, the reconstruction speed reduces. For example, BNFTP introduced another flat white pattern for direct-current (DC) background removal, with which spectral aliasing can be well avoided. Recently, TFTP, short for temporal FTP [26], was proposed, which measures the phase of a pixel by applying Fourier filtration to its e signals. To completely get rid of the spatiotemporal dependency, Zuo et al. developed a μFTP [10] framework based on BNFTP and projection distance minimization (PDM) temporal phase unwrapping (TPU). μFTP requires six patterns of micro-frequency shifts for three frames of 3D reconstruction, where every two successive patterns are used for both phase retrieval and disambiguation. However, all FTP methods are with uncertain accuracy due to inherit spectral filtration, where fringe-modulated base-frequency components are aliasing with DC or their conjugate components.

PSP, differs from FTP mainly in phase retrieval processes, where phase values of each pixel are calculated independently through a temporal analysis of several phase-shift (PS) patterns. In 2006, Zhang et al. [27] developed the first real-time digital-light-processor (DLP)-based PSP of 40 Hz based using three steps of PSs. Various modified PS algorithms were proposed later, such as the "2+1" phase-shifts and Hilbert transforms [28, 29], which were developed for dynamic sensing and must be disambiguated. However, PS-resolved phases are wrapped within 2π and must be disambiguated, for which temporal phase unwrapping methods were developed, including binocular stereo matching, phase coding, and multi-band (frequency) unwrapping. For example, Heist et al. [7] developed the famous 1333Hz GOBO 3D technology using an aperiodic fringe sequence for unambiguous binocular matching; Jiang et al. [32] built 1200 Hz PSP for glass resonance-crushing 3D imaging, based on binocular geometrical constraints (GC). Yin et al. [33] embedded a speckle pattern into four-step PS (4-PS) patterns to achieve unambiguous stereo matching with GC, and this was optimized by Qian et al. [17] and Liu et al. [34] later, where an adaptive GC and 3-PS-embded speckle patterns were used for faster sensing with motion error control. Binocular methods are fast, but they require additional costs, e.g., camera hardware and corresponding point determination calculation with constrained conditions. If a depth constraint is used, in particular, the range of measurement may reduce to a limited one corresponding to a 2π phase domain [16, 35].

Regarding phase coding, Wang et al. [36] proposed a four-pattern-based fringe-period-coded (CPS) PS algorithm for unwrapped absolute phase retrieval. Hyun and Zhang [37] developed 667 Hz PSP by projecting two additional staircasing patterns for phase coding and disambiguation. Chen et al. [38] established a self-coding algorithm for high-speed measurement using four phase-shift patterns only. Wu [39] developed an robust phase measurement framework based on Gray-coded PS. Recently, Cao et al. [40] proposed to use only one extra unequally phase-coded pattern, i.e. 3+1 patterns in total, for fast dual-band phase unwrapping. Phase coding disambiguation requires additional one, two, or more patterns of projection, depending on accuracy requirements, are easily with spike phase-jump errors at the boundaries of coding words resulting in a computational burden.

In contrast, temporal phase unwrapping (TPU) methods using multi-band fringes show widely endorsed accuracy with limited spike errors [22]. Multi-band methods include three sub-groups: heterodyne approaches [41], hierarchical approaches [42], and number theory approaches [43]. Hierarchy approaches have the most robust performance, for which readers can refer to [12, 13, 21] for more details. In 2010, Liu et al. [44] developed a multiplex dual-frequency hierarchical scheme with five PS patterns for absolute phase retrieval. During 2011-13, Wang and Zhang [45, 46] established tri-band 3-PS ("3-3-3") heterodyne and dual-band ("3-3") hierarchy PMP for live rabbit heart imaging, using optimal-pulse-width-modulated DLP projection. Zuo et al. [47, 48] optimized hierarchical and number theory approaches with reduced pattern numbers for faster sensing. For example, a "2-2" approach [47] was developed using two high-band PS patterns plus two reversely set ramp patterns, where a background map obtained from an average of ramp patterns was shared for high-band PS phase trivial. A "3-2" bi-frequency scheme [48] was later developed for pseudo-1250 Hz PMP, where a low-band 3-PS pattern was deleted by sharing a background map from a high-band set and then using a number-theory look-up-table (LUT) for prompt phase unwrapping. Speckle and FTP-assisted TPU methods were developed using fewer patterns [36]. In 2013, Zhang et al. proposed embedding a random speckle to 3-PS patterns instead of adding patterns for phase disambiguation [49]. However, it requires regional similarity voting for CD, indicating that an intensive computation overhead is demanded. In 2016, Li et al. [50] combined FTP with PSP for dynamic imaging using "1-3" dual-band patterns and some improved models [17, 51] were also developed. For example, Qian et al. [17] proposed a hybrid "1-3" method by replacing a high-band FTP pattern using a flat white for BNFTP. However, Qian used single-band fringes, requiring binocular GC for phase unwrapping, resulting in additional hardware and computational overhead.

Nevertheless, these pattern-reduced approaches, including CPS, have limited accuracy due to uncertain spectral aliasing problems and limited coding signal-to-noise ratios. Attributing to the high-accuracy performance [13] and compatibility with limited DLP flash storages, e.g., ≤2 RGB images for DLP4500, "3-3" hierarchical TPU PMP are accepted as a "standard" [12] approach nowadays. For industrial higher accuracy applications, e.g., in-line manufacturing metrology, hierarchical, heterodyne, or number theory TPU PMP using "3-3-3" or "*N*-*N*-*N*" tri-band *N*-step phase-shift (*N*-PS) patterns are preferred [2, 10, 52].

This article has been accepted for publication in IEEE Transactions on Instrumentation and Measurement. This is the author's version which has not been fully edited and content may change prior to final publication. Citation information: DOI 10.1109/TIM.2024.3428592

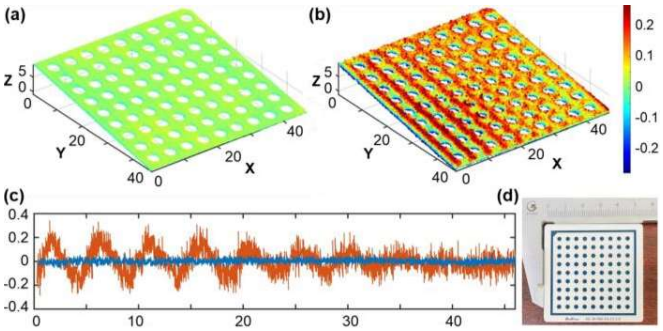

Fig. 1. Hierarchical 3-PS TPU 3D reconstruction of a calibration plate. (a) Using tri-band patterns with FPNs of 1, 8, and 64, with an RMS error of 17.3 μm, (b) using dual-band patterns with FPNs of 1 and 8, with an RMS error of 91.8 μm, (c) their extracted profiles at Y = 25 mm after linear form removal, and (d) a showcase of the measured plate (Units: mm)

B. Contribution

Generally, the fewer patterns used in TPU PMP, the less accuracy is obtained. Take tri-band 3-PS hierarchical TPU PMP as an example. If the band multiplier is M, indicating that fringe period numbers (FPNs) or frequencies are 1, M^2, M^3, respectively, and if the phase-shift phase acquisition error is Gaussian of a standard deviation (SD) σ_φ, the final height error of measurement can be derived using the first-order differential of the classical phase-height model [19], i.e.

$$\sigma_3 = \frac{2\pi L_0 LWM^2}{(\Delta\varphi + 2\pi LM^2)^2} \approx \frac{c_0 W}{2\pi c M^2}\sigma_\varphi \tag{1}$$

where W is the width of the field-of-view (FoV) of a PMP system, $L = cW$ is the length of a system baseline, $L_0 = c_0 W$ is the working distance from the baseline to a reference plane, $\Delta\varphi \approx 0$ is the measured phase difference of a surface from the reference plane, while c_0 and c are proportional constants. For example, if TPU with dual-band fringes instead of triple bands is applied, height measurement error increases to $\sigma_2 = M\sigma_3$. Such an error multiplication effect was demonstrated by experiments and shown in Fig. 1, where the 3D reconstruction root-mean-square (RMS) error of a dual-band TPU method is 5.3 times that of a tri-band method. This magnification rate, which was smaller than the expected FPN multiplier 8, could be attributed to significantly reduced intensities of fringe modulation. In the experiment, the 8-FPN fringe images had a dynamic range of 40-255, while the 64-FPN fringes were within 80-210 due to a degenerating modulation transfer function (MTF) of the system at high-frequency regions.

If speed-optimized dual-band TPU is used, e.g., with reduced 5 or 4 patterns, accuracy would reduce further, as stated in [47, 48]. Multi-band PMP may use a larger FPN multiplier to relax the accuracy problem. However, widely existing phase acquisition errors induced from sensor noise, ambient light, and environmental disturbance require that a practical FPN multiplier to be smaller than 10 (or 20 under controlled conditions) to avoid fringe order errors in TPU [13, 53]. Therefore, TPU using tri-band instead of large-multiplier dual-band fringes, has to be used in high-accuracy industrial applications, e.g., GOM ATOS series PMP, where a typical accuracy error of ~10 μm is claimed.

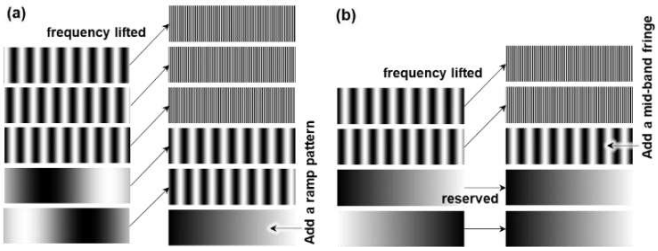

Fig. 2. Two frequency-lift examples based on parameter sharing. (a) Lift of a "3-2" PSP scheme to "3-2-1", and (b) lift of a "2-2" PSP scheme to "2-1-2".

To address the accuracy degeneration problem of speed-optimized dual-band PMP, e.g., the "3-2" bi-frequency scheme [48], we propose a modified "3-2-1" PMP based on fringe FPN or frequency lifting. As presented in Fig. 2(a), "3-2-1" lifts a dual-band scheme to high-accuracy tri-band ones by simply adding an extra fringe pattern of projection, where the background intensity map and fringe modulation map are shared for uses across different-band phase calculations. A typical "3-2-1" scheme includes three high-band PS fringe patterns, two mid-band PS patterns, and a low-band ramp pattern. With a total pattern number of ≤6, "3-2-1" is compatible with most DLP devices without expensive buffer reading overhead. The parameter-sharing-based frequency lift strategy can also be adapted to other dual-band TPU schemes. Take Zuo's "2+2" [47] scheme, for example; a modified "2-1-2" scheme can be developed, as presented in Fig. 2(b). In the developed scheme, two high-band PS patterns, a mid-band fringe pattern, plus two ramp patterns are used for triple-band TPU, based on background and modulation sharing. However, five or fewer patterns are not recommended for accuracy-focused PMP because tri-band fringe modulations may vary dynamically at different object locations.

The "3-2-1" scheme's parameter-sharing philosophy is straightforward. To make it stably work, however, additional calibration work is required regarding fringe blur, nonlinear camera responses, and fringe order error controls. These associated procedures, in terms of their impact on final 3D imaging performance, are carefully investigated in this paper. Our simulations and experiments show that "3-2-1" produced a 42%-85% RMS error reduction from general dual-band methods, depending on dual-band FPN multipliers, with a typical value of 47 μm, but has an equivalent sensing speed using 6 patterns of projection only.

II. Method

A. N-Step Phase-Shifts

The method of phase-shift or PS, widely used in laser interferometer wave-front analysis, plays a vital role in the phase acquisition of PMP. PS converts a set of sinusoidal fringe patterns with constant or random phase shifts from a grayscale domain to a phase domain, which can thus be used for absolute CD and 3D ranging. Usually, 3, 4, or more steps of PS are adopted to extract uniquely a phase map.

In PMP, an ideal fringe image cast to an object's surface will deform when observing at another viewing angle. Given a set

This article has been accepted for publication in IEEE Transactions on Instrumentation and Measurement. This is the author's version which has not been fully edited and content may change prior to final publication. Citation information: DOI 10.1109/TIM.2024.3428592

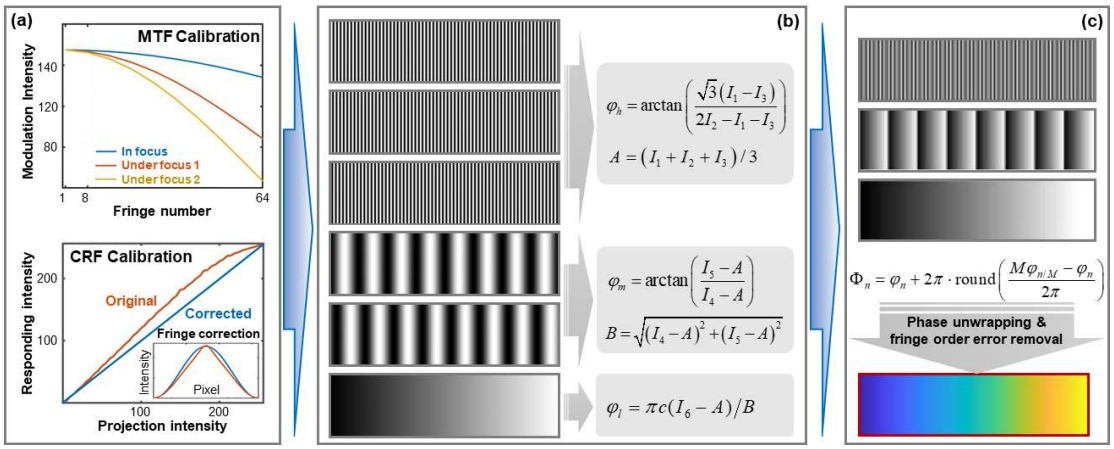

Fig. 3. Framework of "3-2-1" PMP. a) Calibrating the MTF and CRF of a system; b) projecting "3-2-1" fringe patterns with MTF and CRF compensation for wrapped phase acquisition; and c) unwrapping phase maps and removing order errors for absolute phase calculation.

of N-step sinusoidal fringe patterns with a constant PS amount of $2\pi/N$, the received images can be expressed as [12]:

$$I_n(x,y) = A(x,y) + B(x,y)\cos\left(\Phi(x,y) + 2\pi n/N\right) \tag{2}$$

where $A(x,y)$ is the background intensity determined by the average luminous flux of a projector, ambient light, and object reflectivity at a pixel location (x,y); $B(x,y)$ is the fringe modulation intensity which is determined by projection patterns, object defocus, and the inherit optical modulation characteristic of a PMP system; $\Phi(x,y)$ is the phase uniquely determined by its local surface heights; $n = 1,2,\ldots N$ is a PS step number. Providing with $N \geq 3$ steps of PSs, the unknown variables A, B, and φ can be uniquely determined using a least-square manner, using the analytical solution [12]:

$$\varphi(x,y) = -\arctan\left[\frac{\sum_{n=1}^{N} I_n \sin(2\pi n/N)}{\sum_{n=1}^{N} I_n \cos(2\pi n/N)}\right] \tag{3}$$

Specifically, if a minimum step number of 3, i.e., 3-PSs, is adopted, which is preferred in most speed-focused cases, we have the following concise solutions:

$$\begin{aligned} A &= (I_1 + I_2 + I_3)/3, \\ B &= \sqrt{(I_1 - I_3)^2/3 + (2I_2 - I_1 - I_3)^2/9}, \\ \varphi &= \arctan\left[\sqrt{3}(I_1 - I_3)/(2I_2 - I_1 - I_3)\right], \end{aligned} \tag{4}$$

where pixel indices (x,y) are omitted for conciseness.

However, it must be noticed that the inverse solution of arctan yields phase values φ wrapped within [-π, π], resulting in retrieved phase maps with 2π discontinuities and ambiguous in subsequent CD and 3D reconstruction. Basically, a wrapped phase has a multiple of 2π phase jump from the original absolute phase, i.e.

$$\Phi(x,y) = \varphi(x,y) + 2\pi k(x,y) \tag{5}$$

where $k(x,y)$ is the fringe order (or phase order) number at a pixel location. A phase disambiguation or unwrapping process then follows to determine k for each pixel, e.g., using TPU. Hence, the original phase map Φ uniquely associated with object surface heights can be recovered.

B. "3-2-1" Phase Retrieval Based on A-B Sharing

The "3-2-1" TPU PMP, or "3-2-1" simply, is developed based on 3-PSs. It can be understood as an optimized version of a standard "3-3-3" tri-band 3-PSP [52]. Specifically, standard 3-PS high-band, 3-PS mid-band, and 3-PS low-band fringe patterns are replaced by 3-PS high-band, 2-PS mid-band fringe patterns, plus a low-band ramp pattern, as shown in Fig. 3(b). The first three high-band patterns are used for wrapped principal-phase acquisition, while the remaining median/low-band patterns are used for phase unwrapping. "3-2-1" can be further combined with other optimized PS schemes, e.g., by replacing a high-band pattern with a flat white or using Hilbert transforms [28, 29] for motion-resulted phase error control. The basic philosophy of "3-2-1" is to share parameters, including a background intensity map A and fringe modulation intensity map B (short for A-B sharing), across different-band PS calculations. The parameter sharing idea can be used for fringe frequency lift of other PSP schemes, e.g., lift of Zuo's "2+2" [47] scheme to a "2-1-2" scheme, as shown in Fig. 2(b).

A complete "3-2-1" PMP framework is presented in Fig. 3. The framework includes a) two steps of calibration regarding system MTFs and camera response functions (CRFs), b) three steps of phase calculations, and c) a final step of TPU with fringe order error removal. Assume a set of "3-2-1" fringe patterns are projected, and their deformed images acquired from another viewing angle have the following forms:

$$\begin{aligned} I_1(x,y) &= A_h(x,y) + B_h(x,y)\cos\left[\Phi_h(x,y)\right], \\ I_2(x,y) &= A_h(x,y) + B_h(x,y)\cos\left[\Phi_h(x,y) + 2/3\,\pi\right], \\ I_3(x,y) &= A_h(x,y) + B_h(x,y)\cos\left[\Phi_h(x,y) + 4/3\,\pi\right], \\ I_4(x,y) &= A_m(x,y) + B_m(x,y)\cos\left[\Phi_m(x,y)\right], \\ I_5(x,y) &= A_m(x,y) + B_m(x,y)\cos\left[\Phi_m(x,y) + \pi/2\right], \\ I_6(x,y) &= A_l(x,y) + B_l(x,y)\cdot\Phi_l(x,y)/\pi, \end{aligned} \tag{6}$$

where Φ_h, Φ_m, and Φ_l denote respectively the absolute phase maps of the high-band, mid-band, and unit-band patterns, determined uniquely by the surface geometry of a measured object; A_h, A_m, and A_l denote their corresponding background

This article has been accepted for publication in IEEE Transactions on Instrumentation and Measurement. This is the author's version which has not been fully edited and content may change prior to final publication. Citation information: DOI 10.1109/TIM.2024.3428592

intensities, while B_h, B_m, and B_l denote corresponding fringe modulation intensities. Basically, the nine unknown variables cannot be solved from six equations. By sharing A and B, however, "3-2-1" allows to solve the variables smartly according to Algorithm 1.

There are two critical assumptions in "3-2-1" that need to be carefully considered. First, we suppose the background intensity maps are equalized, i.e., $A = A_h = A_m = A_l$, which has been widely accepted in most recent studies. It must be noticed that, however, different band patterns in this scheme use different gray levels at a pixel location, indicating that the obtained phase values and background intensities are with errors if nonlinear camera responses exist [54]. Therefore, nonlinear camera responses of a PMP system must be compensated to enable A's sharing uses. Second, the lower-band fringe modulation intensity maps are supposed to be constantly proportional, e.g., $B = B_m = c \cdot B_l$, with $c < 1.0$ normally. In practice, the MTF of a PMP system is usually imperfect, resulting in different-band fringe images having different modulation intensities, and the modulation difference may vary at different imaging locations and object distances [55]. Thus, the rationality of setting a constant proportion factor c among the fringe patterns could be uncertain, and the varying MTFs must be calibrated. To make the "3-2-1" phase retrieval process robust to varying conditions, additional operations regarding system calibration, compensation, and correction are necessary, as shown in Fig. 1 (a) and (c).

ALGORITHM 1. "3-2-1" PHASE RETRIEVAL BASED ON A-B SHARING.

1) Providing input fringe images of nonlinear CRF compensation, calculates the background intensity map A for sharing uses by assuming that $A = A_h = A_m = A_l$, and wrapped phase map φ_h from high-band fringe images using the standard 3-PS (4);
2) Calculate the modulation intensity map B for sharing uses by assuming $B = B_m = c \cdot B_l$, and the relaying wrapped phase map φ_m from mid-band fringe images using:
$$\varphi_m = -\arctan\left[(I_5 - A)/(I_4 - A)\right], \quad B = \sqrt{(I_4 - A)^2 + (I_5 - A)^2}, \tag{7}$$
where c is a correction factor inherent to a PMP system;
3) Calculate the unit-band auxiliary phase map φ_l from the ramp pattern using
$$\varphi_l = \pi c (I_6 - A)/B; \tag{8}$$
where c is a constant compensating MTF-resulted fringe modulation differences.
4) Shift φ_l, φ_m, and φ_h to the range of $[0, 2\pi)$ by simply augmenting with π and then unwrap them successively to Φ_h for an absolute phase output, through
$$\Phi_n = \varphi_n + 2\pi k = \varphi_n + 2\pi \cdot \mathrm{round}\left(\frac{M\Phi_{n/M} - \varphi_n}{2\pi}\right) \tag{9}$$
by setting $\Phi_1 = \varphi_l$, where n denotes the FPN, and M is the FPN multiplier between adjacent-band fringe patterns.

* Pixel indices (x, y) of each variable are omitted for conciseness.

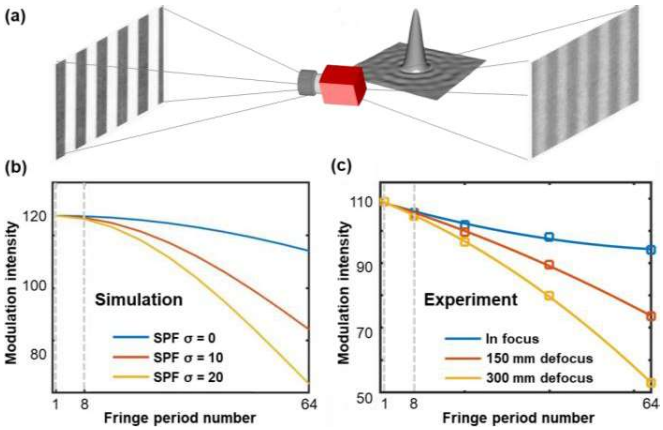

Fig. 4. MTF analysis of an imaging system. (a) Principle of PSF filtration on contrast modulation; (b) theoretical MTFs simulated by convolution with Gaussian PSFs of different kernel sizes; and (c) practically calibrated MTFs tested using sinusoidal fringe images at three axial positions.

C. Modulation Transfer Function Calibration

A modulation transfer function or MTF [55, 56], is the most accepted criterion for imaging quality evaluation. MTF plays a vital role in the design and evaluation of an optical system, such as a simple singlet, multi-element camera, regarding its contrast resolution or resolving power. MTF quantifies the performance of a system by analyzing its amplitude response to various spatial-frequency components of an object. It considers factors such as diffraction, scattering, aberrations, and other optical imperfections, allowing us to understand how a system handles light of various spatial frequencies. Due to the wave nature of light, imaging formation is generally considered a linear shift-invariant filtering process [57]. As such, an optical system is defined by a point spread function (PSF) in a spatial domain, while MTF can be calculated as its magnitude Fourier transform. As presented in Fig. 4(a), the PSF of a camera system behaves as a Gaussian low-pass filter so that a square wave fringe turns to blur and sinusoidal-like, with reduced magnitudes of contrast modulation. The PSF filtration process indicates that low-band components are usually with higher contrast.

The PSF filtering behavior was simulated in terms of sinusoidal patterns with different FPNs, and the resulting modulation magnitude responses, i.e., MTFs, were presented in Fig. 4(b). In the simulation, a set of 3-PS fringe images with different FPNs, e.g., 1, 2 … 64, were generated for testing. They were set with a resolution of 1440×1080 pixels and a full gray-level range within 0-255. Normalized Gaussian PSFs with a kernel size, or SD, of 10, 20, and 30 pixels were then generated and convoluted with the test images. The fringe modulation of each frequency pattern were finally calculated using (4), and the MTFs corresponding to different PSFs were plotted. The simulation results in Fig. 4(b) indicate that the MTF of a Gaussian PSF is also Gaussian, centered at frequency 0. Therefore, if any two MTF samples are obtained, e.g., at FPNs of 8 and 64, a whole MTF curve can be estimated. This deterministic behavior inspired the corrected sharing algorithm in Algorithm 1.

The MTF of a practical PMP system is complex and usually

This article has been accepted for publication in IEEE Transactions on Instrumentation and Measurement. This is the author's version which has not been fully edited and content may change prior to final publication. Citation information: DOI 10.1109/TIM.2024.3428592

a product of its comprising components, including that of a projector, detector, relaying optics, and electronics. Apart from diffraction, a practical MTF might be influenced by factors including F-number, pupil obstruction, aberration, object defocus, field position, and axial location of the image plane of interest. Hence, a practical MTF is usually not Gaussian [55]. Practical MTF calibration methods have been developed, such as point-, line-, and edge-spread function tests with Fourier transforms, or direct measurement using square/sinusoidal-wave targets or bar targets. In the study, DLP-generated sinusoidal-wave patterns were used for the MTF calibration of a homemade PMP system. Specifically, a set of 3-PS sinusoidal patterns with FPNs of 1, 8, 20, 40, and 64 were generated. They were set to have a full gray-level range within 0~255. By setting a constant shutter properly to avoid overexposure, the PS patterns were successively projected to a focused white plate and captured. The fringe modulation intensities were then analyzed using (4). As presented in Fig. 4(c), the fringe modulation intensities at each pixel were calculated and averaged for MTF plotting. Similarly, defocus MTFs were analyzed by setting the test white plate at two defocused positions, e.g., 150 mm, and 300 mm further away from the focus position. The MTFs in Fig. 4(c) show that the fringe modulation intensity decreases along with an increased FPN or defocus depth. Also, the defocus MTFs do not share a common function, e.g., the decreasing trend of the in-focus MTF becomes gentle in a high FPN region of >20, while that of defocus MTFs becomes steep. However, a crucial finding is that the MTF values at FPNs 1 and 8 are nearly constant, with a proportion $c = 0.94 \pm 0.01$. Therefore, a common modulation intensity map can be shared across the low- and mid-band PS calculations, providing a constant correction factor using (8).

D. Camera Response Function Compensation

Camera response function or CRF, i.e., the radiometric response function of a camera, describes how sensor irradiance transforms to measured pixel intensity values of a camera [58]. CRFs are typically nonlinear due to nonlinear optoelectronic conversion efficiency, saturation effects, and electronic noise in a photo-electron production process of photo-sensitive materials. In a PMP system, CRFs are also influenced by projector response functions (PRF), object reflectivity, ambient light, and A/D conversion in projection-imaging processes [59]. Nonlinear CRFs result in received structured light patterns biased from their designed shapes. Hence, subsequently PS-extracted information through (4), including background maps A, modulation maps B, and phase maps φ, are with nonlinear errors [60]. In "3-2-1", the sharing uses of distorted A and B maps in Algorithm 1 further amplify the nonlinear effects. Hence, CRF-reduced nonlinear phase errors must be carefully compensated.

A CRF test regarding our camera, FLIR BFS-US-13Y3M, was conducted first using the prevalent exposure varying method [61]. Consider an ideal camera imaging system; the brightness or intensity recorded by a pixel should be linearly related to scene radiance L and shutter duration t according to:

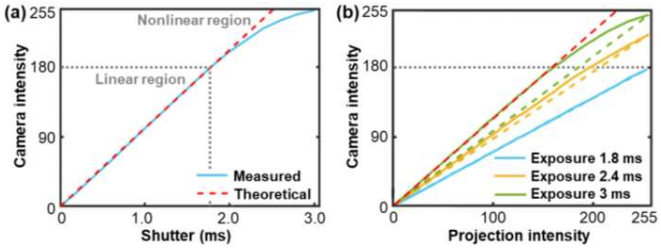

Fig. 5. Demonstration of nonlinear CRF and linear PRF. (a) CRF versus shutter duration, and (b) PRFs versus projection intensities. Dashed lines denote ideal linear responses; beneath dotted lines are linear responses.

$$I = Et = L\frac{\pi}{4}(\frac{d}{f})^2 \cos^4\phi \cdot t \tag{10}$$

where d is the aperture diameter; f is the focal length of the imaging lens; ϕ is the principal ray angle related to the optical axis; and E is the received irradiance in a unit of lux, i.e., lm/m^2. Unfortunately, the final obtained brightness is related via a nonlinear response function, e.g., $M = f(I)$. Therefore, measuring a series of response M at a static scene by simply increasing shutter t or exposure $e = (\pi d^2/4)t$ can quantify the CRF. As presented in Fig. 5(a), a CRF was obtained by recording image intensities at the center-FoV 10×10 pixels using different shutters, through a constant white (255/8-bits) projection uniformly at a static whiteboard with a fixed aperture stop and gain, in a dark room environment. Fig. 5(a) indicates that when the shutter is <1.8 ms, the CRF $f(\cdot)$ is nearly linear with a gray level of <180. When the shutter increases to >1.8 ms, the CRF becomes decurved, due to the effect of optoelectronic saturation as observed in [62].

Fig. 5(a) also indicates that the linear CRF region of a <1.8 ms shutter can be used to test the nonlinearity of a PRF, i.e., the relationship between output intensities of projection and designed projection pattern intensities, according to the typical projector-camera intensity transfer function [54]:

$$I^c = \alpha(r(p(I^{in}) + a_1) + a_2) = \alpha r \cdot p(I^{in}) + b \tag{11}$$

where I^c and I^{in} are respectively the intensity acquired by a camera and the designed intensity of projection; r and α denote, respectively, a constant albedo of a test object and the linear response coefficient of a camera CRF; α_1 and α_2 denote ambient light resulted offsets, $p(\cdot)$ denotes a PRF. In the PRF test, 52 flat white patterns with uniform gray levels of 0, 5, 10, …, 255 were sequentially [12] projected to a whiteboard using a DLP4500-PRO. Camera images were then recorded using the same condition as the previous CRF test. By setting the camera shutter successively to 1.8 ms, 2.4 ms, and 3.0 ms, the projector-camera system response functions (SRF) were recorded, as presented in Fig. 5(b). Since (11) indicates that any nonlinearity of received SRF originate from the PRF $p(\cdot)$, the blue straight line demonstrates that the PRF of the DLP projector is linear. The green SRF curve shows a similar form as the nonlinear CRF in Fig. 5(a), indicating that the SRF nonlinearity comes mainly from the nonlinear CRF.

It is noticeable that the above finding contradicts some existing studies, e.g., in [12, 54]. They mentioned that the nonlinearity of an SRF mainly originates from the PRF because

This article has been accepted for publication in IEEE Transactions on Instrumentation and Measurement. This is the author's version which has not been fully edited and content may change prior to final publication. Citation information: DOI 10.1109/TIM.2024.3428592

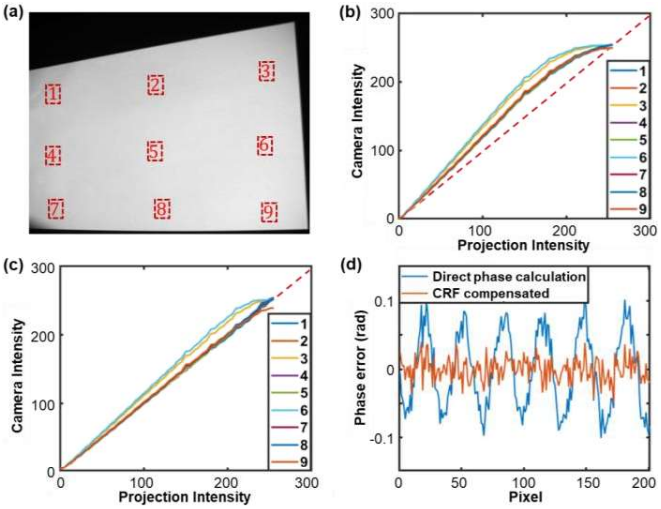

Fig. 6. Performance of CRF nonlinearity compensation. (a) Nine locations of testing, (b) their calibrated CRFs, (c) compensated CRFs using the compensation LUT calibrated at location no. 5, and (d) corresponding phase errors at location no. 5 with and without nonlinear CRF compensation, calculated using standard tri-band 3-PS measurement of a white plate compared to a 12-PS method.

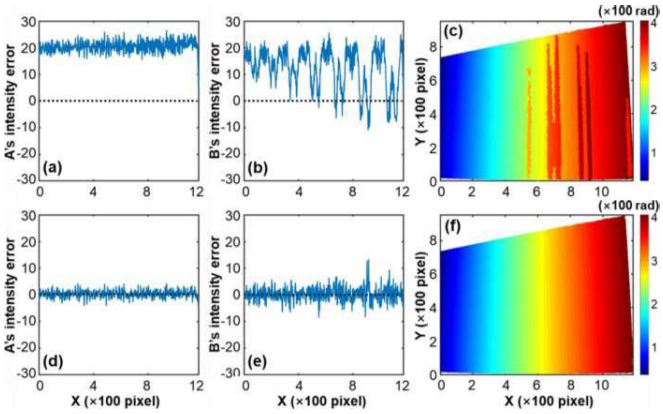

Fig. 7. "3-2-1" phase measurement performance for a white plate without (top) and with (bottom) nonlinear CRF compensation. (a, d) error profiles of background intensity map A at Y = 320, (b, e) error profiles of modulation intensity map B at Y = 320, and (c, f) corresponding absolute phase maps with and without excessive phase-jump errors. The error profiles were extracted by comparing them with the corresponding parameter maps A and B, obtained from a standard tri-band 12-PS measurement.

commercial projectors are designed to meet the nonlinear sensitivity of human vision. They attributed the nonlinear response of a whole PMP system to a projector by assuming that CRF is linear. However, the proof of nonlinear CRF and linear PRF in Fig. 5 is straightforward. This could be attributed to the fact that in the "pattern mode", a DLP projector linearly maps projection intensity to the pulse-width-modulation of vibrating micro-lens, and this can be easily controlled using logic circuits.

With the nonlinear CRF demonstrated, compensation for robust A-B sharing was then tested. We reused the 52 captured images in the previous PRF experiment with a shutter of 3.0 ms for the compensation analysis. The CRFs of nine typical positions, as shown in Fig. 6(a), in the FoV were analyzed individually, as plotted in Fig. 6(b). The results show that the field positions of no. 6 and 3 had the maximum nonlinearity, and then position no. 9 followed. These could be attributed to the fact that these positions had near-specular reflection, so they are pre-saturated due to excessive projector radiance. We used a simple compensation scheme in the test by calibrating a gray-level compensation LUT. The LUT was made as the difference between the CRF of location no. 5 from an ideal CRF, e.g., the red dashed line in Fig. 6(b). Then all the 52 images were compensated using the LUT at each pixel and the LUT-compensated CRFs at the nine locations are plotted in Fig. 6(c). It can be found that the CRF nonlinearities of most areas were suppressed, though no. 6 and 3 have visible residuals. In Fig. 6(d), the phase errors before and after compensation at location no. 5, calculated from a standard tri-band 3-PS pattern set [52], are plotted. Using a 12-PS result as the reference, the compensated RMS phase errors were reduced to 0.09 rad, nearly a 70% reduction from the original 0.29 rad without CRF compensation.

The "3-2-1" algorithm was then tested using the proposed calibration results for compensated phase acquisition. A direct phase measurement and an MTF-corrected, CRF-compensated phase measurement were conducted, respectively, following Algorithm 1, where the tri-band FPNs were set to 64, 8, and 1, while all the other experimental equipment and conditions were the same as that mentioned previously in this section. The obtained intensity maps A and fringe modulation intensity maps B regarding their central error profiles, and absolute phase maps Φ were analyzed, and the results are shown in Fig. 7 In the test, the results from a standard tri-band 12-PS measurement, including a high-band background intensity map and a mid-band fringe modulation map, were used as the reference in the error analysis. The results show that without CRF compensation, the obtained background intensity map A was about 20 gray levels higher than the expected one, and the modulation intensity map B was about 10 higher than the expected one. But the latter oscillated with a frequency twice the mid-band fringe patterns due to the 2-PS algorithm described by (7) used. B's oscillations result in vertical-stripe-like phase-jump errors observed in the finally unwrapped absolute phase maps in Fig. 7(c). By using the proposed CRF compensation and MTF correction strategy in Algorithm 1, Fig. 7(d-f) shows that the background intensity errors, fringe modulation errors, and absolute phase errors were dramatically suppressed across the whole FoV.

An interesting phenomenon in Fig. 7(c) is that the strip-like phase order errors happen at the locations with the negative modulation error extrema, as seen in Fig. 7(b). This is because in the subsequent unit-band phase calculation, i.e., step (3) of Algorithm 1, the ramp pattern modulation map $(I_6 - A)$ and shared modulation map B both had errors, and they were neutralized in the calculation. Specifically, the ramp pattern was designed to have high (>100) gray levels at the mid-to-right region, where highly convex nonlinearity existed, as shown in Fig. 6(b). It results in positively-biased modulation errors because modulation errors are proportional to the concavity of a CRF. Hence, the positively biased modulation error

This article has been accepted for publication in IEEE Transactions on Instrumentation and Measurement. This is the author's version which has not been fully edited and content may change prior to final publication. Citation information: DOI 10.1109/TIM.2024.3428592

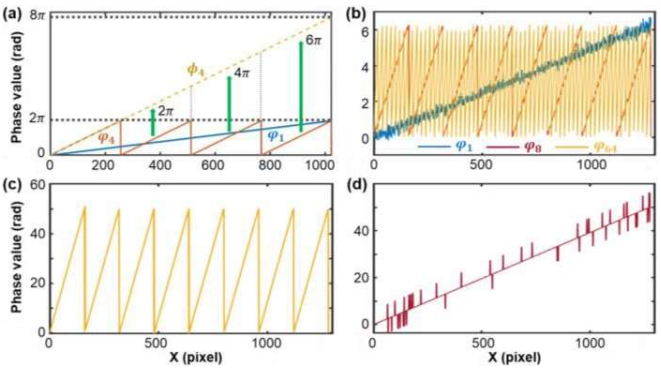

Fig. 8. Simulated FOEs in "3-2-1" TPU. (a) The principle of multi-band TPU, (b) tri-band wrapped phase profiles (with FPNs of 64, 8, 1) of a plate, (c) unwrapped high-band phase from the mid-band one, (d) unwrapped mid-band phase from the low-band one with excessive 2π phase-jump errors.

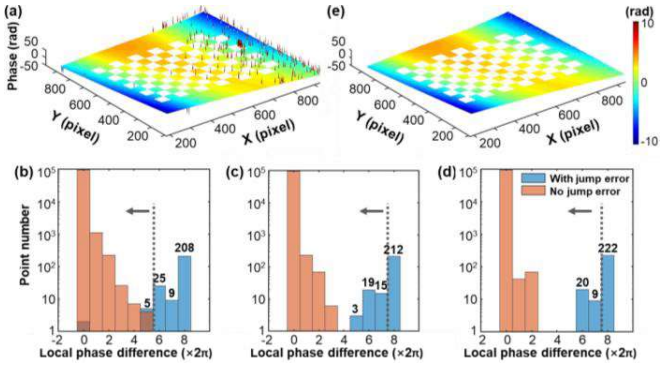

Fig. 9. Local phase difference statistics for robust, probabilistic FOER. (a) A measured checkerboard phase map after leveling, (b-d) phase difference histograms regarding local mean for all FOE points and FOE-free points, using a window of 3×3, 5×5, and 7×7, respectively, and (e) a robustly filtered phase map via 3-neighborhood thresholding using a threshold of 10π.

neutralization effect, in turn, resulted in excessive unit-band phase errors and subsequent TPU phase order errors at the regions with negative modulation error extrema.

E. Fringe Order Error Removal

Equation (9) shows that in multi-band TPU, lower-band phase errors will be amplified with a fringe multiplier M. If a magnified error is close to or exceeds π, a fringe order error (FOE) Δk of calculation that is usually 1 or -1 happens, though multi-band TPU was reported to have the best accuracy [13, 53]. Integral FOEs result in unwrapped phase maps with 2π or $2M\pi$ jump errors [63]. Phase-jump errors are especially common in places with poor fringe signal quality. In the "3-2-1" PS TPU scheme, imperfect MTF correction and CRF compensation may result in residual errors in A-B sharing. For example, simply using the calibrated CRF at location no. 5 in Fig. 6(a) for full-field compensation results in residual nonlinearities, as shown in Fig. 6(c). In practical situations where object motion or defocus exist, correction imperfections could be more complex. These imperfections result in enlarged errors when acquiring mid-band and low-band phase maps. The former φ_m is calculated using two mid-band PS patterns plus an approximate background map A obtained from high-band calculations, while the latter φ_l is calculated using only a ramp pattern plus two approximate maps, including A, and a fringe modulation map B obtained from mid-band PS calculations. Therefore, the obtained phase maps, especially the low-band one, in "3-2-1" are with more significant errors than standard tri-band 3-PSP.

The decreasing phase map accuracy results in that the "3-2-1" scheme is prone to FOEs, and this has been demonstrated using the simulation results in Fig. 8. In the simulation, an ideal "3-2-1" fringe pattern image set with FPNs of 64, 8 and 1 was generated first. The fringe images had a full dynamic range of 0~255 with common Gaussian noise added. Then, a "3-2-1" algorithm was conducted. Because the simulation did not consider the influence of an MTF or CRF, the calculation was straightforward without compensation. Fig. 8(b) shows that the extracted wrapped phases have gradually increased errors along with FPN decreasing, consistent with the previous analysis. Fig. 8(c-d) indicates that due to the substantial errors, TPU from a low-band phase profile to a mid-band one is easily with spike-like phase-jump errors caused by FOEs, while from a mid-band to a high-band is relatively stable.

Various FOE correction methods were developed, including mainly post-correction and pre-avoiding methods mainly [63]. The former has better adaptability and can be applied in all phase unwrapping methods in PMP. However, they are usually statistical, such as median and Gaussian filtering [64], indicating that they may fail if complex situations happen, e.g., when measuring discontinuous and moving objects. Pre-avoiding methods were developed to avoid phase-jump errors fundamentally. However, they usually require additional patterns of projection and are only applicable to specific PS schemes. A recent methodological review of FOE removal (FOER), especially those induced by motion, such as modulation consistency [65], can be referred to [13, 66]. In this session, for "3-2-1" PMP, we proposed a fast, simple, but robust K-neighborhood thresholding algorithm for phase-jump error removal from a probabilistic view.

A median filter, unlike Gaussian or a convolution filter, is designed to remove outliers by filtering a pixel using its local median. Thus, it is nonlinear and could suppress the influence of an outlier completely on its neighbor pixels [64]. To maximize the performance of a median filter, statistical behaviors of phase-jump errors were investigated. For this purpose, a black/white checkerboard was measured using "3-2-1". The checkerboard simplified jump-error identification and had abundant edge discontinuities so that the obtained statistics are applicable to complex object measurement. As presented in Fig. 9(a), a measured phase map shows a large number of spike-like phase-jump errors, especially at the edge discontinuity locations. Due to the existence of projection and imaging distortion, obtained patterns were with non-uniform fringes, resulting in unwrapped phase maps slightly bending, as shown in Fig. 9(a). A simple π-thresholding was applied to the leveled phase map for FOE identification. The correctness of the identification was further confirmed by comparing with a manual observation. Then, the phase differences of each error and error-free pixel from its local mean, i.e.

$$\Delta\Phi_{\Omega_-} = \Phi - \mathrm{mean}(\Phi_{\Omega_-}) \tag{12}$$

This article has been accepted for publication in IEEE Transactions on Instrumentation and Measurement. This is the author's version which has not been fully edited and content may change prior to final publication. Citation information: DOI 10.1109/TIM.2024.3428592

were calculated, where Ω- denotes the index set of local pixels within a window, excluding the analyzing pixel itself. By counting their occurring frequencies, the histograms in Fig. 9(b-d) indicate that a large filtering window results in a large histogram separation of the error and error-free points. The statistics indicate that a simple $\Delta\Phi_\Omega$ threshold can be used for reliable FOER when a large filtering window is used.

The local phase maps of the error points with minor $\Delta\Phi_\Omega$ were carefully checked. We found that all the local maps corresponding to the blue columns on the left of the dashed lines in Fig. 9(b-d) had not-a-number (NaN) values. This finding indicates that a relatively large threshold, e.g., those denoted by the dashed lines, can be used for correct FOER because their local phase differences are NaNs, and simultaneously, those error-free points can be reserved as much as possible. Based on the statistical analysis, a robust neighborhood-thresholding algorithm was proposed for FOER, as in Algorithm 2. Fig. 9(e) presents an FOE-free filtered result by simply setting the window size to 3 and the safety threshold to 10π. More reliable results can be obtained by increasing the window size K and tuning the safety threshold $\kappa\pi$ with $\kappa = 1, 2, 3, \ldots, 2(M-1)$.

ALGORITHM 2. K-NEIGHBORHOOD THRESHOLDING FOR FOE REMOVAL.

1) Providing with an absolute phase map Φ and corresponding modulation map B obtained from Algorithm 1, mask Φ by setting $\Phi(B > B_0) = \text{NaN}$, where $B_0 = 15$ used in the study is a predefined threshold;
2) Construct a K-by-K neighborhood filtration kernel Θ of all values of $1/(K^2-1)$ but a central zero, and calculate a neighborhood-filtered phase map $\widetilde{\Phi}$ by convoluting Φ using the kernel, i.e., $\widetilde{\Phi} = \Phi \otimes \Theta$;
3) Calculate the absolute local phase difference map using $\Delta\Phi_{\Omega-} = |\Phi - \widetilde{\Phi}|$ and identify the jump-error-free point index set Λ by checking if $\Delta\Phi_{\Omega-} < \kappa\pi$, where $\kappa = 10$ used in the study is a predefined safety margin;
4) Remove phase-jump errors by setting $\Phi(\sim\Lambda) = \text{NaN}$.

III. SIMULATIONS

A complete "3-2-1" PMP loop with MTF/CRF correction and FOE removal was simulated for theoretical demonstration of the proposed method based on the setup shown in in Fig. 11(a). The phase measurement accuracy of "3-2-1" was also verified compared to some state-of-the-art methods. Thus, the accuracy limit of the proposed method could be predicted. In the simulation, a set of ideal "3-2-1" fringe images of FPNs 64, 8, and 1 were generated using (6) at first. The images were set with a full dynamic range of 0-255, and a resolution of 1280×720. Assuming a PMP system with a perfectly leveled MTF and linear CRF, the ideal projection images could be simply used as the final captured images for phase recovery. Hence, a direct "3-2-1" phase calculation was conducted via Algorithm 1 without MTF/CRF compensation. The results in Fig. 10(a-c) show that the finally obtained phase map and intermediate results, including background intensity and fringe modulation maps, are correct.

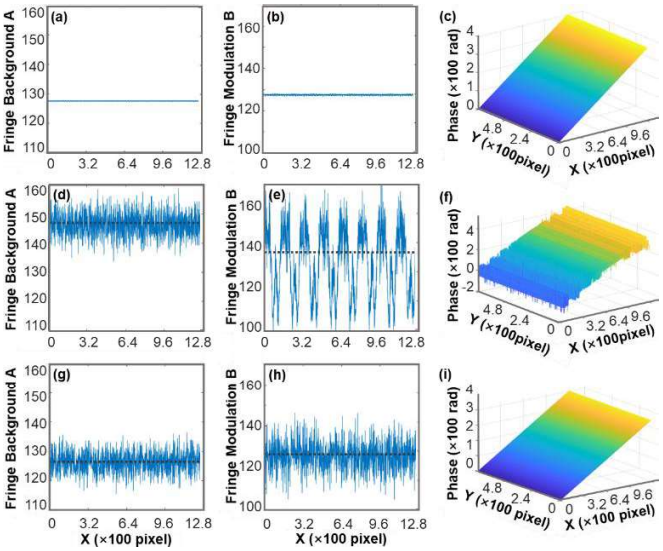

Fig. 10. "3-2-1" PMP simulation for a plane measurement. (a-c) Direct "3-2-1" TPU calculation from an ideal "3-2-1" fringe image set without compensation, (d-f) corresponding direct calculation from a "3-2-1" image set added with artificial MTF/CRF distortions and Gaussian noise, and (g-h) corresponding calculation through a compensated "3-2-1" calculation using Algorithm 1. Black dashed lines denote means.

Then, an MTF and CRF calibrated in previous studies were applied to the "3-2-1" pattern images. Specifically, we artificially reduce the fringe magnitude of the mid-/high-band fringes according to the red curve in Fig. 4(a), and then distort their pattern intensities according to no. 5 curve in Fig. 6, following which Gaussian noise with an SD of 6 was finally added. Without MTF/CRF compensation, direct "3-2-1" phase calculation, the same as the previous step, was applied. The results in Fig. 10(d-f) show that the obtained background map had a uniform lift of ~20 gray levels due to the artificial lifting CRF. The extracted fringe modulation also had a lift due to the CRF convexity. However, the 2-PS phase calculation using (7) resulted in the recovered modulation map B was with a significant oscillation with a frequency twice the mid-band fringes. Attributed to the oscillated fringe modulation error, the finally obtained phase map had significant stripe- and spike-like FOEs that were anti-symmetric to the center of the FoV. These results are consistent with the experimental ones shown in Fig. 7(a-c), where more practical issues, such as non-uniform illumination, field curvature, and other aberrations, resulted in non-uniform FOE distribution across the FoV.

Finally, a complete, compensated "3-2-1" calculation was conducted through Algorithm 1. The results in Fig. 10(g-i) show that after CRF compensation was applied, the obtained background intensity reduced to ~126 with an SD of 2.7, and the recovered fringe modulation intensity also reduced to ~125 with an SD of 5.9, very close to their designed value of 128. With a slight correction of B using a simulating MTF and neighborhood thresholding for FOER, a jump-error-free phase map was finally obtained. The detailed intermediate results demonstrated that the proposed scheme is theoretically complete for reliable phase acquisition. The root-mean-square phase errors (RMSPEs) of "3-2-1" regarding the ideal phase

This article has been accepted for publication in IEEE Transactions on Instrumentation and Measurement. This is the author's version which has not been fully edited and content may change prior to final publication. Citation information: DOI 10.1109/TIM.2024.3428592

map in Fig. 10(c) were analyzed. For comparison, some similar methods, including "3-3-3" [52], "3-3" [46], and "3-2" [48] PSP methods, were also simulated, and their RMSPEs were counted, as presented in Table I.

The results show that the standard "3-3-3" method had the best accuracy. By simply reducing projection patterns, the "3-3" method with a low FPN multiplier resulted in an RMSPE 6.8 times that of "3-3-3". If the FPN multiplier was optimized to 20, which matched with a preset image noise (Gaussian) of SD 3.8 and 3-PS phase noise SD ~0.05 rad, according to [53]:

$$M+1<\pi/(3\sigma)\alpha \tag{13}$$

so that very limited FOEs were resulted, the dual-band methods including "3-3" and "3-2" (with FOER) were found to produced 2.7 times the RMSPEs of "3-3-3". Both error aggravation were slightly smaller than their expectations, i.e., 8 and 3.2, respectively. This phenomenon, consistent with the evidence in Fig. 1, could be attributed to the reduction of fringe modulation of higher-frequency fringes. The "3-2" PSP used only two patterns for a low-band phase's recovery, resulting in increasing phase noise, TPU FOEs, and thus final RMSPE. By applying the proposed FOER method, "3-2" could achieve the same good accuracy as the standard "3-3" PSP. The "3-2-1" scheme used two patterns for mid-band phase recovery and only one for low-band phase recovery, resulting in the worst RMSPE. With FOER applied, however, "3-2-1" achieved the same accuracy as the standard "3-3-3" PSP. In conclusion, "3-2-1" could achieve the same accuracy as standard tri-band methods, but it is less robust due to a reduced pattern number. Therefore, FOER shall be considered as a standard routine in the scheme.

TABLE I RMSPE STATISTICS OF PMP SIMULATIONS.

Method	Pattern number	FPN	RMSPE (rad)
"3-3-3"	9	64, 8, 1	0.034
"3-3" (Low M)	6	8*, 1	0.232
"3-3"	6	20*, 1	0.093
"3-2" (No FOER)	5		3.214
"3-2"	5		0.093
"3-2-1" (No FOER)	6	64, 8, 1 (ramp)	9.820
"3-2-1"	6		0.034

* The FPN multiplier 20 was set to match with the phase error σ of ~0.05 rad in simulation; dual-band absolute phase maps were scaled up by 8 or 3.2 to be comparable with the ideal phase map of Fig. 10(c).

IV. EXPERIMENTS

A. Experimental configuration

A "3-2-1" PMP system (see Fig. 11a) was built to verify the performance of the proposed method. The system comprised a CMOS camera (BFS-US-13Y3M-C) and a DLP projector (DLP3010EVM-LC). The camera had a focal length of 10 mm, a working distance of 400 mm, and a square pixel dimension of 4.8 μm. Camera resolution was semi-sampled to 640×512 so that a higher framerate was enabled. The projector had a calibrated focal length of 8.3 mm, a resolution of 1280×720, and a square pixel dimension of 5.4 μm. The two core devices were synchronized to a maximum framerate of 504 fps, triggered by the DLP projector under its 8-bit depth pattern mode (pre-exposure dark, exposure, and post-exposure dark were respectively 0.17 ms, 1.72 ms, and 0.03 ms). Using six patterns for one frame of 3D reconstruction, the "3-2-1" scheme realized an aliasing-free framerate of 84~126 fps in 3D imaging. The latter higher framerate was achieved through a combining use of Wu's time-overlapping technique [39, 67], where the patterns for fringe order solving, i.e., the mid-/low-band patterns, were repetitively used with different high-band series. If temporal interpolation is allowed, a 504 fps pseudo-framerate is naturally expected. If binary patterns were used with the DLP projector, the 3D imaging rate could be even higher. Before experiments, the system was calibrated using Zhang's method [68], though some other methods are also available [69].

The "3-2-1" PMP method and several state-of-the-art methods were analyzed regarding their imaging precision and robustness against object complexities, such as large object depth, edge discontinuities, and local specular reflections. The robustness was analyzed by evaluating the number of out-of-tolerance or excessive error points (EEPs). Here, an absolute phase pixel with an error of >π was defined as an EEP. EEPs were used for robustness evaluation because the number of EEPs is typically proportional to the object area of complex features. Precisely, the number ratios of EEPs over all valid points were calculated. Their robustness against object motion and environmental variations was outside the scope of the study, though they shall be evaluated in practical applications. The precision was evaluated using the RMS phase errors (RMSPE) from a ground-true map that was obtained using the "12-12-12" method, i.e., standard tri-band 12-PSP with FPNs of 64, 8, and 1. Because all the test methods used the same system calibration parameters, systematical measurement errors introduced by calibration inaccuracy, including lens distortion and artifact imperfections, were neutralized. RMSPEs excluding EEPs were also analyzed to suppress the influence of EEPs as outliers on precision analysis.

The PMP methods of the test included typical "3-3-3", "3-3" and "3-2" PSP, depth-constrained (GC)-3-PSP, μFTP, PS-μFTP, and the "3-2-1" PSP. The "3-3-3" PSP was a standard method with balanced accuracy and speed considerations [52]. The "3-3" PSP [46] was a standard method widely used in high-speed applications. The "3-2" method [48] was speed-optimized for higher-speed applications. Zuo's "2-2" method [47] was not analyzed due to its worst accuracy performance. The GC-3-PSP [35] was a 3-step PSP using a min-depth constraint for absolute phase unwrapping. μFTP [10] used three micro-frequency-shift fringe patterns plus three flat white patterns, i.e., six patterns in total, for BNFTP phase acquisition and absolute phase recovery. All the tri-band methods used the FPNs of 64, 8, and 1; the dual-band method used an FPN multiplier of 20 for precision maximization, according to the phase noise analysis in [53], while a multiplier of 8 was also tested for comparison. The GC-3-PSP used an FPN of 8 to balance its measuring depth and precision. The μFTP method used FPNs of 57, 64, and 73, where the least common multiple 1280 of fringe periods 1280/57, 1280/64, and 1280/73 ensures a full-field absolute phase map was unambiguously recovered.

This article has been accepted for publication in IEEE Transactions on Instrumentation and Measurement. This is the author's version which has not been fully edited and content may change prior to final publication. Citation information: DOI 10.1109/TIM.2024.3428592

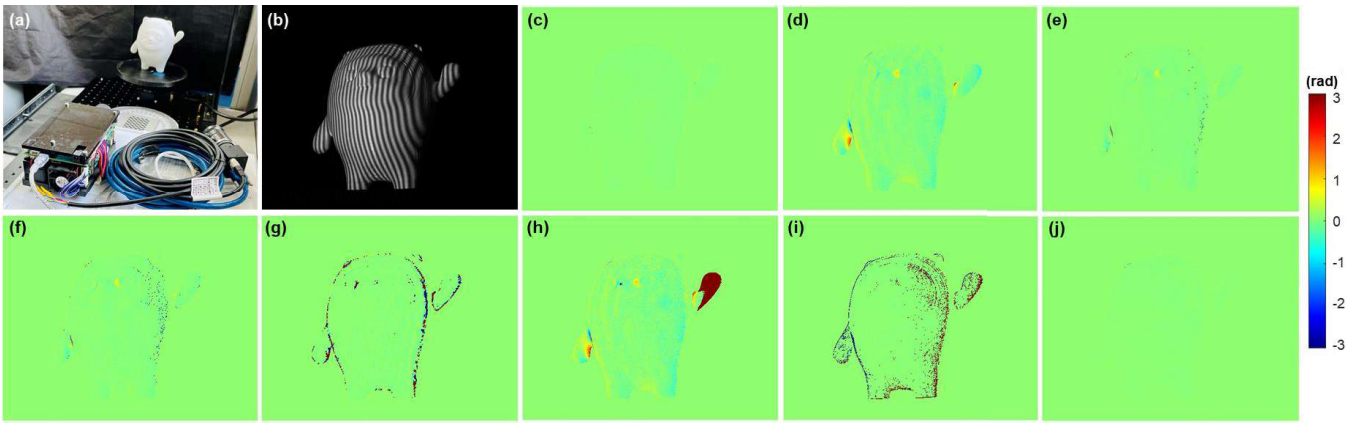

Fig. 11. Measurement results of a 20 cm-tall Bing Dwen Dwen. (a) Experimental setup, (b) a captured fringe image, and measured phase error maps from (c) "3-3-3", (d) "3-3" with a low FPN multiplier, (e) "3-3", (f) "3-2" (g) μFTP, (h) GC-3-PSP, (i) "3-2-1" without FOE control, and (j) "3-2-1" PMP.

B. Precision and robustness analyses – Bing Dwen Dwen

A 20 cm-tall Bing Dwen Dwen 3D-printed nylon model was used for the measurement precision and robustness test. Bing Dwen Dwen is a typical freeform [70] object, a measurement test of which, thus, could comprehensively reveal the capability of the proposed method. As presented in Fig. 11, we show that the standard "3-3-3" PSP had the best robustness performance with nearly invisible EEPs. The "3-2" and "3-3" methods had a few EEPs intensively distributed around the model boundaries. The FTP methods show significant errors, mainly in FOEs around feature edges. This was because edge features were usually with over-high/-low albedos. Thus, significant phase noise and FOEs of phase unwrapping were resulted. The phase-error edge enrichment phenomenon was especially significant in FTP methods due to the wide-band aliasing of discontinuous features in a Fourier domain. The GC-3-PSP exhibited remarkable EEPs at the object's distal features, e.g., the right hand, due to the limited depth range of 1/8 of the other methods. The "3-2-1" method was unstable with significant edge FOEs, but it can result in equivalent high-accuracy results as the standard "3-3-3" PSP using the proposed FOE removal.

The EEP rates, defined as the ratio of the EEP amount to the total number of valid points with a modulation intensity of >15, with the RMSPEs of the tested methods, are summarized in Table II. In particular, the RMSPEs with all EEPs of $>\pi$ excluded, compared to the standard "12-12-12" PMP, were analyzed to disclose the achievable precision limits from an experimental perspective. The results show that "3-3-3" had the best precision with a RMSPE of ~0.05 rad. If a minimal number of FOEs was removed, an expected RMSPE limit of ~0.03 rad was achieved. The dual-band methods, e.g., "3-3" and "3-2", had an EEP-excluded RMSPE of ~0.08 rad, which was 2.6 times that of "3-3-3", while a "3-3" method with a low FPN multiplier of 8 produced an RMSPE of 6.7 times that of "3-3-3". Both limited improvements of "3-3-3" were highly consistent with the simulation evidence obtained in Table II, verifying that the simulation results in session 3 are faithful. However, the directly obtained RMSPEs of the dual-band methods, e.g., ~0.49 rad and 0.90 rad, were much more significant than their expectations because the scaling factor 3.2 also amplified noise. Both μFTP methods produced 2.6 times the precision limits of the standard "3-3-3" method with FOE removal, though they are tri-band methods. This was because μFTP used Fourier transforms for phase acquisition, which is naturally less stable due to unavoidable spectral aliasing. One can see that both μFTP methods produced significant RMSPEs if EEPs were not removed. The GC-3-PSP with an FPN of 8 also produced a precision limit of ~0.21 rad, similar to "3-3" with a low FPN multiplier. The evidence also verified that the previous finding of 6.7-6.8 times the accuracy improvement of general dual-band methods to tri-band ones was reliable. However, the GC-3-PSP had a limited measuring depth, resulting in a significant RMSPE due to the right hand's out-of-range problem of Bing Dwen Dwen, as shown in Fig. 11(f). The proposed "3-2-1" method showed a precision RMSPE limit similar to the standard tri-band "3-3-3" method. With FOE removal applied, "3-2-1" showed a slightly reduced RMSPE down to 0.027 rad. This was because "3-2-1" easily produced FOEs from large-phase-error points, which, however, were removed, thus resulting in the EEP-excluded RMSPE being reduced further. In summary, the experimental results in Table II, which are highly consistent with the previous simulation, demonstrate that the "3-2-1" method can achieve the same precision limit as the standard tri-band 3-PSP, using the proposed MTF/CRF compensation and FOE removal strategies. This was 2.6-6.8 times precision improvement or 62%-85% RMSPE reduction from general dual-band methods, depending on different FPNs, but using an equivalent projection pattern number of 6 only.

TABLE II PRECISION AND ROBUSTNESS STATISTICS (BING DWEN DWEN).

Method	Pattern number	FPN	EEP rate (%)	RMSPE (rad)	RMSPE exc. EEP (rad)
"3-3-3"	9	64, 8, 1	0.001	0.049	0.031
"3-3" (Low *M*)	6	8*, 1	0.050	0.231	0.208
"3-3"	6	20*, 1	0.023	0.489	0.082
"3-2"	5		0.057	0.904	0.082
μFTP	6	57, 64, 73	0.588	8.690	0.080
GC-3-PSP	3	8	0.899	9.168	0.212
"3-2-1" (No FOER)	6	64, 8, 1 (ramp)	0.844	10.005	0.030
"3-2-1"	6		0.001	0.051	0.027

This article has been accepted for publication in IEEE Transactions on Instrumentation and Measurement. This is the author's version which has not been fully edited and content may change prior to final publication. Citation information: DOI 10.1109/TIM.2024.3428592

* Dual-band absolute phase maps were scaled up by 8 or 3.2 to be comparable with the reference phase map obtained using the standard tri-band 12-PSP.

C. *Results and analyses – Chckerboard*

A checkerboard artefact as presented in Fig. 12 was used to further verify the precision and robustness demonstrated previously. Checkerboard artefacts are widely used for camera calibration due to the high manufacturing accuracy, and the convenience of manual operation and computation. Therefore, this test is a good reference for future comparative studies. For this purpose, the same routine as in session IV.B was conducted and the EEPs, RMSPEs, and RMS height errors (RMSEs) in particular, were analyzed, as presented in Table III. Height RMSEs can enable comparative studies in a dimensional space.

Table III shows that the dual-band PSP with different FPN multiples produced RMSPEs of 4.8 and 2.1 times that of "3-3-3", respectively. These were smaller than that of Bing Dwen Dwen case, due to most likely the improved dual-band fringe image quality of the plane object. Table III also indicates that the height RMSEs of the system were approximately linear to RMSPEs with a factor of 1.30 mm/rad. A final RMS precision of 0.047 mm was obtained for the 300 mm-FoV home-made PMP. This precision could be reduced further if more steps of phase shifts are used or a smaller FoV is applied. Anyway, this study verified the previous simulation and Bing Dwen Dwen study. It demonstrated that the "3-2-1" method could achieve equivalent precision as the standard tri-band 3-PSP, showing a 42%-75% RMSPE reduction from general dual-band methods, but using an equivalent projection patterns number of 6 only.

TABLE III PRECISION AND ROBUSTNESS STATISTICS (CHECKERBOARD).

Method	EEP Rate (%)	RMSPE (rad)	RMSPE exc. EEP (rad)	RMSE (mm)	RMSE exc. EEP (mm)
"3-3-3"	0	0.029	0.029	0.038	0.038
"3-3" (Low *M*)	0	0.140	0.140	0.179	0.179
"3-3"	0	0.062	0.062	0.080	0.080
"3-2"	0	0.062	0.062	0.080	0.080
µFTP	0.062	2.462	0.055	3.291	0.071
GC-3-PSP	0	0.138	0.138	0.178	0.178
"3-2-1" (No FOER)	0.002	0.427	0.036	0.448	0.047
"3-2-1"	0	0.036	0.036	0.047	0.047

V. CONCLUSIONS

In this paper, a precision-retained high-speed 3D imaging method called "3-2-1" PMP was developed. The basic philosophy of the method is to share common parameters, including a background intensity map and fringe modulation intensity map across different-band phase-shift calculations. The parameter-sharing philosophy is straightforward. To make it stably work, however, additional calibration work is required regarding system modulation transfer, nonlinear camera responses, and fringe order error controls. These associated procedures, in terms of their impact on final 3D imaging performance, have been carefully investigated in this paper. The parameter-sharing frequency lift strategy can also be adapted to other dual-band TPU PMP. We suppose that this method is of promising use in extreme applications with both high speed and accuracy requirements.

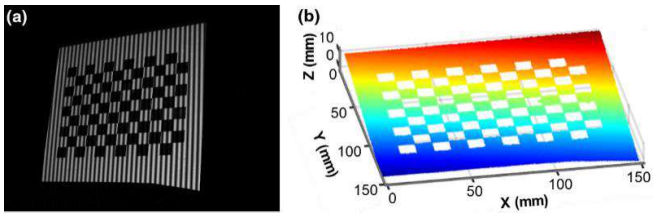

Fig. 12. Measurement test of a checkerboard. (a) A captured fringe image, (b) 3D reconstruction using standard "12-12-12" PSP.

Simulations and experiments were conducted. They consistently demonstrated that show that the "3-2-1" PMP has an equivalent precision as the standard tri-band 3-step-phase-shift PMP. It produced a 42%-85% root-mean-square error reduction from general dual-band methods and famous µFTP, depending on object complexities and fringe-period-number multipliers, with a typical value of 47 µm which is 0.015% relative to a 300 mm field-of-view, but using an equivalent projection pattern number of 6 only, or even less. The homemade 504 fps projection-rate system realized a temporally aliasing-free 3D imaging framerate of 84 fps. The framerate can simply achieve 126 fps using the recently proposed time-overlapping technique, or even higher if defocused projection are applied.

REFERENCES

[1] Y. Hu, Z. Liang, K. Wang, K. Gui, J. Zhang, Q. Chen, and C. Zuo, "Structured light 3D imaging instrument for biological tissues with potential application in telemedicine," *IEEE T. Instrum. Meas.,* vol. 73, p. 5001411, 2024.

[2] Y. Liu, L. Blunt, Z. Zhang, H. A. Rahman, F. Gao, and X. Jiang, "In-situ areal inspection of powder bed for electron beam fusion system based on fringe projection profilometry," *Addit. Manuf.,* vol. 31, p. 100940, 2020.

[3] L. Hinz *et al.*, "Fringe Projection Profilometry in Production Metrology: A Multi-Scale Comparison in Sheet-Bulk Metal Forming," *Sensors,* vol. 21, no. 7, p. 2389, 2021.

[4] Y. Zheng, S. Wang, Q. Li, and B. Li, "Fringe projection profilometry by conducting deep learning from its digital twin," *Opt. Express,* vol. 28, no. 24, pp. 36568-36583, Nov 2020.

[5] Y. Lu, G. Sun, X. Xiao, and J. Mazumder, "Online Stress Measurement During Laser-aided Metallic Addit. Manuf.," *Sci. Rep.,* vol. 9, no. 1, p. 7630, 2019.

[6] J.-S. Hyun, G. T. C. Chiu, and S. Zhang, "High-speed and high-accuracy 3D surface measurement using a mechanical projector," *Opt. Express,* vol. 26, no. 2, pp. 1474-1487, 2018.

[7] S. Heist, P. Dietrich, M. Landmann, P. Kuhmstedt, G. Notni, and A. Tunnemann, "GOBO projection for 3D measurements at highest frame rates: a performance analysis," *Light Sci. Appl.,* vol. 7, p. 71, 2018

[8] H. Wu, Y. Cao, Y. Dai, and H. Li, "Dynamic 3D measurement based on temporal fringe order recognition," *IEEE. T. Instrum. Meas.,* vol. 72, p. 5028412, 2023.

[9] L. Fu *et al.*, "Binary Fringe Defocused Projection Technology: A Review," *Laser Optoelectron. Prog.,* vol. 59, p. 1415011, 2022.

[10] C. Zuo, T. Tao, S. Feng, L. Huang, A. Asundi, and Q. Chen, "Micro Fourier Transform Profilometry (µFTP): 3D shape measurement at 10,000 frames per second," *Opt. Lasers Eng.,* vol. 102, pp. 70-91, 2018.

[11] F.B.D. Dizeu, J. Boisvert, M.-A. Drouin, G. Godin, M. Rivard, G. Lamouche, "Frequency shift method: A technique for 3D shape acquisition in the presence of strong interreflections," *IEEE T. Instrum. Meas.,* vol. 71, p. 7004919, 2022.

[12] C. Zuo, S. Feng, L. Huang, T. Tao, W. Yin, and Q. Chen, "Phase shifting algorithms for fringe projection profilometry: A review," *Opt. Lasers Eng.,* vol. 109, pp. 23-59, 2018.

[13] C. Zuo, L. Huang, M. Zhang, Q. Chen, and A. Asundi, "Temporal phase unwrapping algorithms for fringe projection profilometry: A comparative review," *Opt. Lasers Eng.,* vol. 85, pp. 84-103, 2016.

[14] Y. Zhang, Y. Sun, N. Gao, Z. Meng, and Z. Zhang, " Phase target-based calibration of projector radial chromatic aberration for color fringe 3D measurement systems," *Sensors,* vol. 22, p. 6845, 2022.
[15] Budianto, D. P. K. Lun, and Y. H. Chan, "Robust Single-Shot Fringe Projection Profilometry Based on Morphological Component Analysis," *IEEE T. Image Process.,* vol. 27, no. 11, pp. 5393-5405, 2018.
[16] Z. Li, K. Zhong, Y. F. Li, X. Zhou, and Y. Shi, "Multiview phase shifting: A full-resolution and high-speed 3D measurement framework for arbitrary shape dynamic objects," *Opt. Letters,* vol. 38, no. 9, pp. 1389-1391, 2013.
[17] J. Qian, T. Tao, S. Feng, Q. Chen, and C. Zuo, "Motion-artifact-free dynamic 3D shape measurement with hybrid Fourier-transform phase-shifting profilometry," *Opt. Express,* vol. 27, no. 3, pp. 2713-2731, 2019.
[18] C. Zuo *et al.*, "Deep learning in optical metrology: a review," *Light Sci. Appl.,* vol. 11, no. 1, p. 39, 2022.
[19] S. Chen "Calibration of intraoral 3D measurement system with using consummated model combined with highly accurate data pairs," *IEEE T. Instrum. Meas.,* vol. 72, p. 4507813, 2023.
[20] H. Zhou, M. M. R. Hussain, and P. P. Banerjee, "A review of the dual-wavelength technique for phase imaging and 3D topography," *Light Adv. Manuf.,* vol. 3, no. 2, pp. 314-334, 2022.
[21] Z. Wu and Q. Zhang, "High-Speed 3D Topography Measurement Based on Fringe Projection: A Review," *Laser Optoelectro. Prog.,* vol. 60, no. 8, p. 0811001, 2023.
[22] S. Zhang, "High-speed 3D shape measurement with structured light methods: A review," *Opt. Lasers Eng.,* vol. 106, pp. 119-131, 2018.
[23] X. Su and W. Chen, "Fourier transform profilometry:: a review," *Opt. Lasers Eng.,* vol. 35, no. 5, pp. 263-284, 2001.
[24] Q.-C. Zhang and X.-Y. Su, "An optical measurement of vortex shape at a free surface," *Opt. Laser Technol.,* vol. 34, no. 2, pp. 107-113, 2002.
[25] Z. Qican, H. Lei, C. Yao-Wei, K. Lau-Gih, and A. Anand, "4D metrology of flapping-wing micro air vehicle based on fringe projection," in *Proc. SPIE*, 2013, vol. 8769, p. 87692Y.
[26] Y. Liu, Q. Zhang, H. Zhang, Z. Wu, and W. Chen, "Improve Temporal Fourier Transform Profilometry for Complex Dynamic Three-Dimensional Shape Measurement," *Sensors*, vol. 20, no. 7, p. 1808, 2020.
[27] Z. Song and S. H. Peisen, "High-resolution, real-time three-dimensional shape measurement," *Opt. Eng.,* vol. 45, no. 12, p. 123601, 2006.
[28] Z. Song and Y. Shing-Tung, "High-speed three-dimensional shape measurement system using a modified two-plus-one phase-shifting algorithm," *Opt. Eng.,* vol. 46, no. 11, p. 113603, 2007.
[29] Y. Wang, Z. Liu, C. Jiang, and S. Zhang, "Motion induced phase error reduction using a Hilbert transform," *Opt. Express,* vol. 26, no. 26, pp. 34224-34235, 2018.
[30] Z. Zhang, S. Huang, S. Meng, F. Gao, and X. Jiang, "A simple, flexible and automatic 3D calibration method for a phase calculation-based fringe projection imaging system," *Opt. Express,* vol. 21, no. 10, pp. 12218-12227, 2013.
[31] S. Zhang, "Recent progresses on real-time 3D shape measurement using digital fringe projection techniques," *Opt. Lasers Eng.,* vol. 48, no. 2, pp. 149-158, 2010.
[32] C. Jiang, P. Kilcullen, Y. Lai, T. Ozaki, and J. Liang, "High-speed dual-view band-limited illumination profilometry using temporally interlaced acquisition," *Photon. Res.,* vol. 8, no. 11, pp. 1808-1817, 2020.
[33] W. Yin *et al.*, "High-speed 3D shape measurement using the optimized composite fringe patterns and stereo-assisted structured light system," *Opt. Express,* vol. 27, no. 3, pp. 2411-2431, 2019.
[34] P. Zhou, Y. Cheng, J. Zhu, J. Hu, " High-dynamic-range 3D shape measurement with adaptive speckle projection through segmentation-based mapping," *IEEE T. Instrum. Meas.,* vol. 72, p. 5003512, 2022.
[35] Y. An, J.-S. Hyun, and S. Zhang, "Pixel-wise absolute phase unwrapping using geometric constraints of structured light system," *Optics Express,* vol. 24, no. 16, pp. 18445-18459, 2016.
[36] Y. Wang, K. Liu, Q. Hao, D. L. Lau, and L. G. Hassebrook, "Period Coded Phase Shifting Strategy for Real–time 3-D Structured Light Illumination," *IEEE T. Image Process.,* vol. 20, no. 11, pp. 3001-3013, 2011.
[37] J.-S. Hyun and S. Zhang, "Superfast 3D absolute shape measurement using five binary patterns," *Opt. Lasers Eng.,* vol. 90, pp. 217-224, 2017.
[38] P. Liu, K. Zhang, B. Zhao, M. Li, and Y. Chen, " Self-coding phase shift for absolute phase retrieval in fringe projection profilometry," *IEEE T. Instrum. Meas.,* vol. 72, p. 5026610, 2023.
[39] Z. Wu, W. Guo, Y. Li, Y. Liu, and Q. Zhang, "High-speed and high-efficiency three-dimensional shape measurement based on Gray-coded light," *Photon. Res.,* vol. 8, no. 6, pp. 819-829, 2020.
[40] H. An, Y. Cao, Y. Zhang, and H. Li, " Phase-shifting temporal phase unwrapping algorithm for high-speed fringe projection profilometry," *IEEE T. Instrum. Meas.,* vol. 72, p. 5009209, 2023.
[41] J. M. Huntley and H. Saldner, "Temporal phase-unwrapping algorithm for automated interferogram analysis," *Appl. Opt.,* vol. 32, no. 17, pp. 3047-3052, 1993.
[42] H. Zhao, W. Chen, and Y. Tan, "Phase-unwrapping algorithm for the measurement of three-dimensional object shapes," *Appl. Opt.,* vol. 33, no. 20, pp. 4497-4500, 1994.
[43] Z. Jingang and W. Ming, "Phase unwrapping by lookup table method: application to phase map with singular points," *Opt. Eng.,* vol. 38, no. 12, pp. 2075-2080, 1999.
[44] K. Liu, Y. Wang, D. L. Lau, Q. Hao, and L. G. Hassebrook, "Dual-frequency pattern scheme for high-speed 3-D shape measurement," *Opt. Express,* vol. 18, no. 5, pp. 5229-5244, 2010.
[45] Y. Wang and S. Zhang, "Superfast multifrequency phase-shifting technique with optimal pulse width modulation," *Opt. Express,* vol. 19, no. 6, pp. 5149-5155, 2011.
[46] Y. Wang, J. I. Laughner, I. R. Efimov, and S. Zhang, "3D absolute shape measurement of live rabbit hearts with a superfast two-frequency phase-shifting technique," *Opt. Express,* vol. 21, no. 5, pp. 5822-5832, 2013.
[47] C. Zuo, Q. Chen, G. Gu, S. Feng, and F. Feng, "High-speed three-dimensional profilometry for multiple objects with complex shapes," *Opt. Express,* vol. 20, no. 17, pp. 19493-19510, 2012.
[48] C. Zuo *et al.*, "High-speed three-dimensional shape measurement for dynamic scenes using bi-frequency tripolar pulse-width-modulation fringe projection," *Opt. Lasers Eng.,* vol. 51, no. 8, pp. 953-960, 2013.
[49] Y. Zhang, Z. Xiong, and F. Wu, "Unambiguous 3D measurement from speckle-embedded fringe," *Appl. Opt.,* vol. 52, no. 32, pp. 7797-7805, 2013.
[50] B. Li, Z. Liu, and S. Zhang, "Motion-induced error reduction by combining Fourier transform profilometry with phase-shifting profilometry," *Opt. Express,* vol. 24, no. 20, pp. 23289-23303, 2016.
[51] P. Cong, Z. Xiong, Y. Zhang, S. Zhao, and F. Wu, "Accurate Dynamic 3D Sensing With Fourier-Assisted Phase Shifting," *IEEE J-STSP,* vol. 9, no. 3, pp. 396-408, 2015.
[52] J. Wang, Z. Zhang, W. Lu, and X. J. Jiang, "High-Accuracy Calibration of High-Speed Fringe Projection Profilometry Using a Checkerboard," *IEEE-ASME T. Mech.,* vol. 27, no. 5, pp. 4199-4204, 2022.
[53] J. Wang, Z. Zhang, R. K. Leach, W. Lu, and J. Xu, "Predistorting Projected Fringes for High-Accuracy 3-D Phase Mapping in Fringe Projection Profilometry," *IEEE T. Instrum. Meas.,* vol. 70, p. 5008209, 2021.
[54] S. Zhang and S.-T. Yau, "Generic nonsinusoidal phase error correction for three-dimensional shape measurement using a digital video projector," *Appl. Optics,* vol. 46, no. 1, pp. 36-43, 2007.
[55] G. D. Boreman, *Modulation transfer function in optical and electro-optical systems*, 2nd ed. (Tutorial texts in optical engineering Volume TT121). Bellingham, Washington State: Society of Photo-Optical Instrumentation Engineers, 2021.
[56] C. S. Williams and O. A. Becklund, *Introduction to the optical transfer function* (SPIE Press monograph PM112). Bellingham, Wash: SPIE Press, 2002.
[57] J. M. Coupland and J. Lobera, "Holography, tomography and 3D microscopy as linear filtering operations," *Meas. Sci. Technol.,* vol. 19, no. 7, p. 074012, 2008.
[58] Y. Matsushita, "Radiometric Response Function," in *Computer Vision: A Reference Guide*, K. Ikeuchi Ed. Cham: Springer International Publishing, 2021, pp. 1038-1041.
[59] A. Babaei, M. Saadatseresht, and J. Kofman, "Exponential fringe pattern projection approach to gamma-independent phase computation without calibration for gamma nonlinearity in 3D optical metrology," *Opt. Express,* vol. 25, no. 21, pp. 24927-24938, 2017.
[60] Y. Wang, J. Cai, D. Zhang, and X. Chen, "Nonlinear Correction for Fringe Projection Profilometry With Shifted-Phase Histogram Equalization," *IEEE T. Instrum. Meas.,* vol. 71, p. 5005509, 2022.
[61] T. Mitsunaga and S. K. Nayar, "Radiometric self calibration," in *Proceedings. 1999 IEEE Computer Society Conference on Computer Vision and Pattern Recognition*, 1999, vol. 1, pp. 374-380 Vol. 1.
[62] J. Li, J. Guan, Y. Wang, X. Chen, and J. Xi, "Accurate estimation of camera response function for high dynamic range measurement," *Appl. Optics,* vol. 61, no. 1, pp. 167-176, 2022.
[63] Z. Wu, W. Guo, L. Lu, and Q. Zhang, "Generalized phase unwrapping method that avoids jump errors for fringe projection profilometry," *Opt. Express,* vol. 29, no. 17, pp. 27181-27192, 2021.

[64] M. Storath and A. Weinmann, "Fast Median Filtering for Phase or Orientation Data," *IEEE T. Pattern Anal.,* vol. 40, no. 3, pp. 639-652, 2018.
[65] S. Feng, Q. Chen, C. Zuo, R. Li, G. Shen, and F. Feng, "Automatic identification and removal of outliers for high-speed fringe projection profilometry," *Opt. Eng.,* vol. 52, no. 1, p. 013605, 2013.
[66] L. Lu, V. Suresh, Y. Zheng, Y. Wang, J. Xi, and B. Li, "Motion induced error reduction methods for phase shifting profilometry: A review," *Opt. Lasers Eng.,* vol. 141, p. 106573, 2021.
[67] Z. Wu, W. Guo, Q. Zhang, H. Wang, X. Li, and Z. Chen, "Time-overlapping structured-light projection: high performance on 3D shape measurement for complex dynamic scenes," *Opt. Express,* vol. 30, no. 13, pp. 22467-22486, 2022.
[68] S. Zhang and P. Huang, S., "Novel method for structured light system calibration," *Opt. Engineering,* vol. 45, no. 8, pp. 1-8, 2006.
[69] J. Yu, F. Da, and W. Li, "Calibration for Camera–Projector Pairs Using Spheres," *IEEE T. Image Process.,* vol. 30, pp. 783-793, 2021.
[70] J. Wang, S. Bi, W. Liu, L. Zhou, T. Li, I. Macleod, and R. Leach, Stitching locally fitted T-splines for fast fitting of large-scale freeform point clouds, *Sensors*, vol. 23, p. 9816, 2023